The Astrophysical Journal, 970:161 (13pp), 2024 August 1 https://doi.org/10.3847/1538-4357/ad5314


# Spectral Indices and Evidence of Wave–Wave Modulation in Observations of the Interplanetary Magnetic Field

Paul T. M. Loto'aniu[1,2] and Larisza Krista[1,2]
[1] Cooperative Institute for Research in Environmental Sciences University of Colorado, Boulder Boulder, CO 80309, USA; paul.lotoaniu@noaa.gov
[2] National Centers for Environmental Information National Oceanic and Atmospheric Administration Boulder, CO 80303, USA
*Received 2023 December 27; revised 2024 May 30; accepted 2024 May 31; published 2024 July 29*

## Abstract

We present wave and turbulence observations from the DSCOVR spacecraft during the 2017 September solar flare and coronal mass ejection (CME) events. On September 4–12, the spectral index within the magnetic field power spectral density inertial range was consistent with Kolmogorov $-5/3$. This is despite the 9 days being composed of a complex mix of different features, including solar flares, solar energetic particle events, and CMEs. When analyzing shorter time periods, the spectral index varies. For two days where there were consecutive CMEs, the index follows Kraichnan–Iroshinikov $-3/2$, while on two quiet days, it was a mixture of $-1$, $-3/2$, and $-2$. The inertial range spectral index taken over the entire 9 days hides or averages out spectral features that occur over shorter time periods. We use a more realistic estimate of the amount of Doppler shifting into the spacecraft frame to show that the break frequencies on most days were located close to the H+ cyclotron frequency. We present evidence of wave–wave modulation and suggest that lower-frequency waves in the solar wind can modulate the growth rates/propagation of ion cyclotron waves, providing a method to transfer energy in the solar wind to smaller scales. Furthermore, we suggest that the indices in the inertial range can be explained by combining containment due to wave generation/propagation and stochastic Brownian motion in the solar wind. When these two phenomena are equal, they combine to create a $-3/2$ index.

*Unified Astronomy Thesaurus concepts:* Heliosphere (711); Solar wind (1534); Interplanetary turbulence (830)

## 1. Introduction

The observational evidence for turbulent energy cascade in the solar wind mainly comes from determining the spectral indices of solar wind fluctuations. However, caution should always be taken when considering turbulence spectral indices (Borovsky 2010; Viall & Borovsky 2020). Calculation of the power spectral density (PSD) using the Fast Fourier Transformation (FFT) results in a snapshot of the power averaged over the FFT length at each frequency, and it is challenging to distinguish the different solar wind features contributing to that power. As noted by Viall & Borovsky (2020), the spectral analyses of turbulence in the solar wind often occur without consideration of what specific types of structures (i.e., current sheets, plasma boundaries, magnetic holes, pressure-balance structures, and mirror modes) are in the solar wind time series.

In addition, the interpretation of parallel and perpendicular fluctuations in solar wind turbulence is highly coordinate-frame-dependent. The two directions are defined relative to the background magnetic field, which in the case of the solar wind is the mean interplanetary magnetic field (IMF). Differentiating between parallel and perpendicular fluctuations is important for understanding the nature of solar wind turbulence (Zhao et al. 2020).

Large-scale structures in the magnetic field distort the turbulence scaling law at smaller scales when performing an FFT, which may cause turbulence anisotropy to appear scale-independent (Cho & Vishniac 2000; Milano et al. 2001; Oughton & Matthaeus 2020). Depending on the nature of the structure, it may be possible to average out or flatten its spectra by using a long FFT length. However, this effectively hides evidence of some of the physical processes that are present and compounds the distortion. The selected FFT length can modify the spectral index in the inertial range.

The difficulty of interpreting the solar wind spectral indices further complicates attempts at explaining the lack of consistency in the observed indices, particularly within the inertial range. In this range, observations sometimes match the Kolmogorov (hydrodynamic; Kolmogorov 1941; Kolmogorov et al. 1991) index of $-5/3$, some follow the Kraichnan–Iroshinikov (incompressible MHD; Iroshnikov 1963; Kraichnan 1965) $-3/2$ index, while other values ranging from $-1$ to $-2$ have also been observed. Different extensions of basic MHD turbulence theory have been suggested to explain the indices, and the reader is referred to Bruno & Carbone (2013) for a review of both observations and theories. A more recent review, albeit admittedly biased, but with an excellent summary of current theoretical trends in MHD turbulence, is Schekochihin (2022).

Electromagnetic ion cyclotron (EMIC) waves are commonly observed in the solar wind (e.g., Jian et al. 2009, 2010; He et al. 2011; Podesta & Gary 2011; Wei et al. 2016). EMIC waves are Alfvénic waves occurring below the ion cyclotron frequency and generated through temperature anisotropy during Doppler-shifted ion cyclotron instability (e.g., Gary 1993). The waves are often associated with solar wind ion heating, including at the turbulence dissipation range (e.g., Leamon et al. 1998; Woodham et al. 2018; Bowen et al. 2020). The dissipation range is usually defined by a steepening in the index of the solar wind magnetic field spectra at the higher-frequency edge of the inertial range (e.g., Bruno & Carbone 2013). However, the Doppler shifting of the cyclotron resonance means EMIC waves can also be observed at fractions of the ion cyclotron

frequency (e.g., Jian et al. 2009; Wei et al. 2016) well within the inertial frequency range. Since the solar wind propagates through interplanetary space at supersonic speeds, an additional Doppler shift must be accounted for when moving from the plasma frame to the measuring spacecraft frame (e.g., Jian et al. 2009).

Previous studies within Earth's magnetosphere have found that EMIC wave power can be modulated by longer-period waves (e.g., Mursula et al. 1997; Loto'aniu et al. 2009). We present observations around the 2017 September solar flares that suggest similar wave–wave modulation occurs in the solar wind, and we discuss the possible connection between this mechanism and energy cascade. We also present theoretical ideas based on stochastic arguments to explain the commonly observed spectral indices in the solar wind.

In Section 2, the Deep Space Climate Observatory (DSCOVR), Advanced Composition Explorer (ACE), and Wind data used in the study are described. Section 3 shows the general solar wind conditions during the 2017 September event. Section 4 outlines the process for calculating the spacecraft frame ion cyclotron frequencies, while Section 5 presents the static PSD results. Section 6 shows example EMIC wave events and describes the wave–wave modulation mechanism. In Section 7, the cross-satellite comparisons are shown, while Section 8 describes the stochastic approach. The discussion is presented in Section 9, and Section 10 states our conclusions.

## 2. Data Description

The National Oceanic and Atmospheric Administration (NOAA) DSCOVR mission was launched in 2015 February to the first Lagrange point (L1), where the ACE and Wind spacecraft are both located. DSCOVR is used by NOAA for space weather operations, with ACE as a backup. The science payloads on board DSCOVR include the PlasMag suite (Szabo 2014), which comprises the Faraday Cup and the magnetometer (MAG). Here, we focus on the MAG, which samples the IMF at 50 samples per second.

For a comparison of DSCOVR solar wind data to ACE and Wind, see Loto'aniu et al. (2022). We obtained DSCOVR data from NOAA's National Centers for Environmental Information (NCEI) DSCOVR data portal. The ACE and Wind magnetic field data were obtained from NASA's Coordinated Data Analysis Web. The solar energetic particle (SEP) data comes from the Geostationary Operational Environmental Satellite (GOES)-16 satellite Solar Galactic Proton Sensor (SGPS) data stored at the NOAA-NCEI GOES-R space weather data portal. Links to the NOAA-NCEI data portals are in the acknowledgments.

In terms of the coordinate systems, we present the data in both radial–tangential–normal (RTN) and mean-field-aligned (MFA) coordinates. The RTN system depends on the location of the spacecraft, where R is the vector directed from the Sun toward the spacecraft, T is the cross product of the Sun's polar (heliographic) axis with R, and N is the cross product RxT completing the right-hand coordinates. The MFA coordinates are defined with the $Z$-axis along the IMF mean field (30 minutes running average), while the $Y$ and $X$ axes are orthogonal to $Z$. Converting from RTN to MFA, the $Y$ MFA axis is defined as the cross product of the Sun's polar (heliographic) axis with $Z$, and the $X$ MFA axis the cross product $X$x$Z$ completing the right-hand coordinates.

## 3. Solar Wind Conditions during the 2017 September Solar Flares

The 2017 September 4–10 solar flare period has been extensively studied. See the *Space Weather* journal special issue titled *Space Weather Events of 2017 September 4–10* for a collection of papers on this event. A summary of the space weather impacts can be found in Redmon et al. (2018). Figure 1 shows the general solar wind conditions covering 2017 September 4–17 and the corresponding high-energy proton flux observed by the GOES-16 SGPS instrument. This event period is complex, with multiple flares, SEP events, and coronal mass ejections (CMEs). Furthermore, observations (not presented here) from the Ultra-Low-Energy Isotope Spectrometer (Mason et al. 1998) on board ACE showed that multiple ion species were enhanced during the event, including He+ and O+ (Cohen & Mewaldt 2018). The ion enhancements can provide a source of free energy for EMIC wave generation and amplification (e.g., Chang et al. 1986; Thorne & Horne 1994; Telloni & Bruno 2016).

## 4. Calculation of Ion Cyclotron Frequencies in the Spacecraft Frame

The outward propagation of the solar wind Doppler shifts frequencies associated with motions of comparable speeds or slower. For a spacecraft observer, this is a Doppler shift from the solar wind plasma frame to the relatively stationary spacecraft frame. In order to establish a relationship between solar wind spectral frequencies and ion cyclotron frequencies, careful estimates of the amount of Doppler shifting are required.

Assuming parallel-propagating left-hand (LH) polarized EMIC waves and outward-directed solar wind propagation, an observed LH polarity in the spacecraft frame indicates waves propagating with a propagation vector $k$ antisunward, with $k \cdot V_{sw}$ being positive, where $V_{sw}$ is the solar wind velocity. Alternatively, the observed right-hand (RH) polarity implies sunward-propagating $k$, with $k \cdot V_{sw}$ being negative. Jian et al. (2009) converted the wave frequency in the spacecraft frame ($f_{sc}$) to the solar wind frame ($f_{sw}$) by removing the Doppler shift effect, using

$$f_{sc} = f_{sw} + \frac{k \cdot V_{sw}}{2\pi} = f_{sw}\left(1 + \frac{V_{sw}}{V_A}\hat{k} \cdot \hat{V}_{sw}\right), \quad (1)$$

where $V_A$ is the Alfvén speed.

Usually, studies assume $\hat{k} \cdot \hat{V}_{sw} \sim 1$, which means waves propagating parallel to both the background magnetic field and the direction of the outward-flowing solar wind. Here we allow the angle between the solar wind flow direction and the IMF to vary between 180° and 0°, which means the dot product can vary between −1 and 1. We further assume that in RTN coordinates, the $R$ radial component is directed along the solar wind propagation direction. With these assumptions, we make the approximation $\hat{k} \cdot \hat{V}_{sw} \sim b_r/b$, where $b$ is the background magnetic field and $b_r$ is the radial magnetic field component of the RTN system. Hence, Equation (1) can be rewritten as

$$f_{sc} = \left| f_{sw}\left(1 + \frac{V_{sw}}{V_A}\frac{b_r}{b}\right) \right|, \quad (2)$$

where the absolute sign is to account for the negative frequencies that result from waves traveling in the opposite direction to the solar wind flow direction. If $b_r/b = 0$, then the

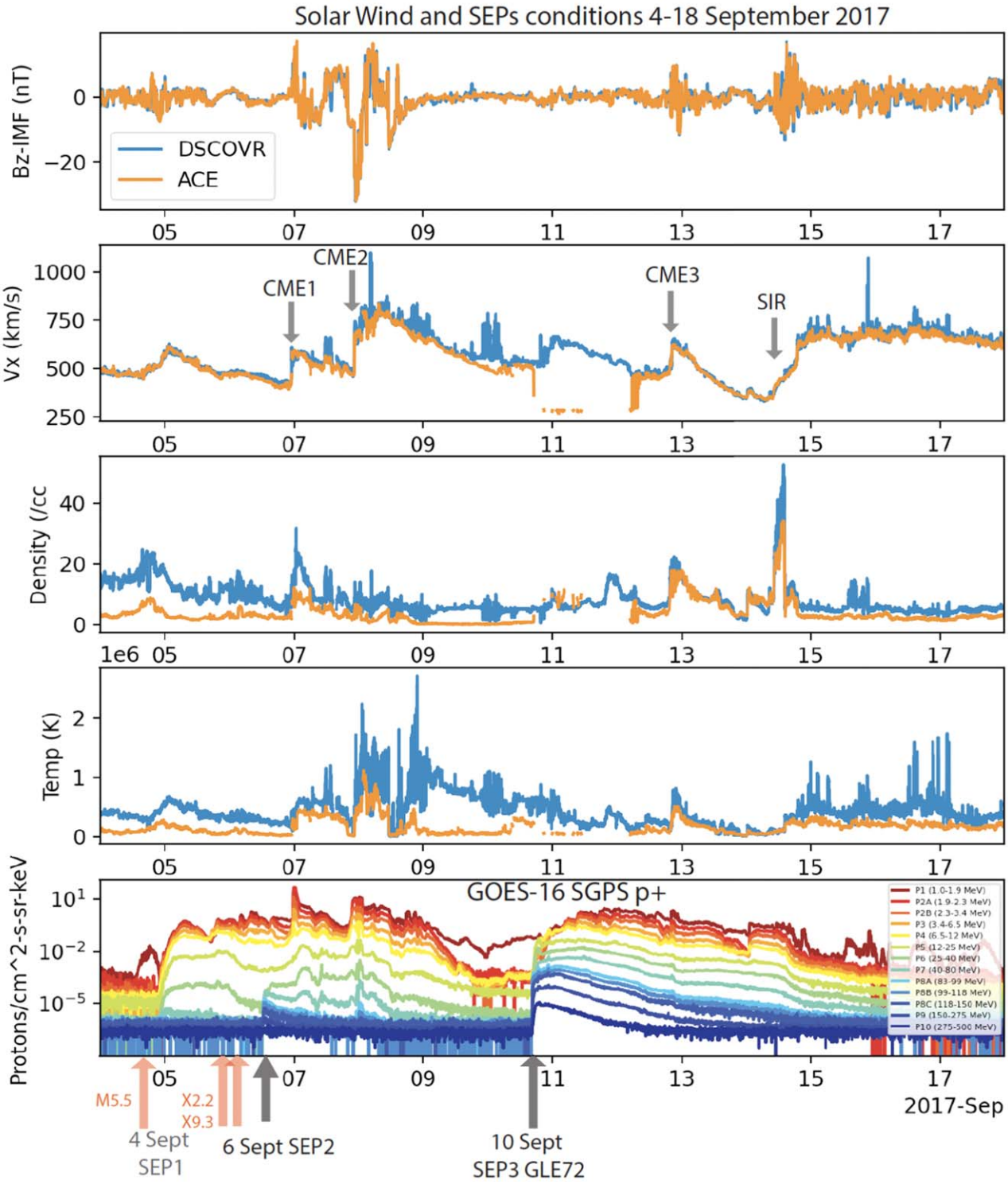


**Figure 1.** Space weather conditions during the 2017 September solar flare events.

wave is not Doppler shifted when observed by the spacecraft, because it is traveling at right angles to the solar wind propagation direction, while if $b_r/b = \pm 1$, there is maximum Doppler shifting when observed by the spacecraft either moving with or opposite to the direction of the solar wind.

The top panel in Figure 2 shows DSCOVR magnetic field data for September 4–12. Panel (b) shows the dynamic PSD of the RTN transverse magnetic field component, $b_n b_n^* + b_t b_t^*$. The H+, He+, and O+ cyclotron frequencies in the plasma frame are overlaid ($\Omega_{\rm pf}^{H+}$, $\Omega_{\rm pf}^{He+}$, and $\Omega_{\rm pf}^{O+}$). The dynamic PSD is constructed from calculating the PSD using the FFT with an appropriate FFT length, then sliding across the time series by a sliding window length and repeating the process until the end of the time series (e.g., Gröchenig 2000).

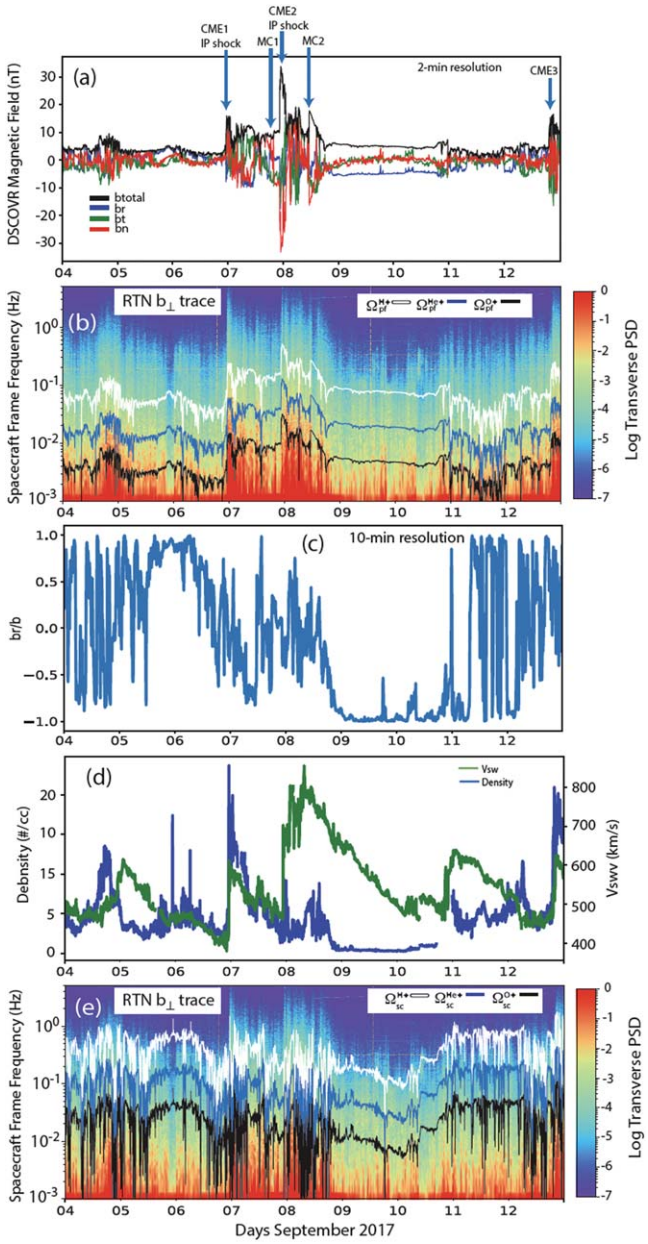


**Figure 2.** The DSCOVR magnetic field in RTN coordinates, time series, the dynamic spectrum with O+ and H+ cyclotron frequencies in the plasma frame, the $b_r/b$ ratio, the solar wind density and speed estimates using Wind and ACE, and the ACE and dynamic spectra but with O+ and H+ cyclotron frequencies and the spacecraft frame.

In order to calculate the cyclotron frequencies in the spacecraft frame, we need to estimate $V_A$ from

$$V_A = \frac{b}{\sqrt{\mu_0 \rho}}, \tag{3}$$

where the plasma density $\rho$ is defined as

$$\rho = \sum_s n_s m_s \tag{4}$$

or the sum of densities of each ion species $s$ having mass density $n_s$ and particle mass $m_s$. However, a heavy ion abundance is rarely high enough to have a significant effect on $V_A$ compared to the H+ abundance. For example, $n_{He}/n_H$ rarely exceeds 5% (Song et al. 2022), while $n_{He}/n_O \sim 44$–$211$ and $n_{Fe}/n_O \sim 0.1$–$0.24$ during corotating interaction regions (CIRs), interplanetary shocks, SEPs, and fast solar wind events (Filwett et al. 2019). Hence, we can assume $\rho = n_H m_H$ in Equation (3). Writing Equation (2) specifically for the ion cyclotron frequency of species $s$ in the spacecraft frame, $\Omega^s_{sc}$, gives

$$\Omega^s_{sc} \sim \left| \frac{Z_s q_e b}{2\pi m_s} \left( 1 + V_{sw} \frac{\sqrt{\mu_0 n_H m_H}}{b} \cdot \frac{b_r}{b} \right) \right|, \tag{5}$$

where $Z_s$ is the charge state of the ion $s$, and $q_e$ is the electron charge.

In Equation (5), $b$, $b_r$, $n_H$, and $V_{sw}$ come from solar wind observations. Figure 2(c) shows the $b_r/b$ ratio from the DSCOVR magnetic field measurements. The multiple CMEs and general increased activity and field rotations during the September 4–12 period result in a ratio that varies dramatically between +1 and −1. The ratio was most stable on September 9 and 10. We use the ratio values shown in Figure 2(c) in Equation (5). Figure 2(d) shows $V_{sw}$ and $n_H$ measured at L1. $V_{sw}$ values are from ACE, while $n_H$ comes from Wind, with about a 14 hr data gap filled with ACE data and another 9 hr gap filled in by simple interpolation. We use Equation (5) to obtain the cyclotron frequencies in the spacecraft frame for H+, He+, and O+ ($\Omega^{H+}_{sc}$, $\Omega^{He+}_{sc}$, and $\Omega^{O+}_{sc}$), which are shown in Figure 2(e), overlaying the dynamic PSD spectra. The Doppler-shifted frequencies show large variations due to the variations in the $b_r/b$ ratio.

## 5. Static PSD Observations

Figure 3 shows the full 50 Hz resolution DSCOVR magnetic field static PSDs. From top to bottom, the figure panels display: (a) the magnetic field trace over 9 days from September 4–12 in both MFA and RTN coordinates; (b) the same time periods as (a), but showing the transverse ($b_\perp$) trace and the parallel component ($b_{||}$) PSD in MFA coordinates; (c) the same as (b), but for September 7–8; (d) the same as (c), but for September 9–10; (e) the $b_r/b$ ratio time series for 14:30–15:30 UT on September 7; and (f) the corresponding $b_{||}$ PSD in MFA and $b_r$ PSD in RTN. Curves with indices ranging from −2 to −1 are also shown.

In Figure 3, we also show the mean $\Omega^{H+}_{sc}$ and $\Omega^{He+}_{sc}$. These values were calculated by first estimating the cyclotron frequency in the spacecraft frame at each time stamp, as described in Section 4, summing them, and then averaging by dividing by the FFT length. There are artificial signals observed starting around 3 Hz, probably due to spacecraft interference. However, as shown in panel (f), they are weak signals peaking around 10 $\mathrm{pT}/\sqrt{\mathrm{Hz}}$.

As shown in panel (a), over the entire 9 days, the field traces in RTN and MFA coordinates both follow **−5/3** in the inertial range, before steepening into the dissipation range starting close to $\Omega^{H+}_{sc(mean)} \sim 0.39$ Hz. In MFA coordinates, $b_\perp$ and $b_{||}$ also follow **−5/3**. Although difficult to see on the scale shown in panel (b), the power in $b_\perp$ was generally higher throughout the inertial range compared to $b_{||}$.

CME1 and CME2 were observed by DSCOVR at L1 on September 7 and 8. Figure 3(c) shows that over September 7–8, the inertial range spectral index in MFA coordinates for both $b_\perp$ and $b_{||}$ follows a Kraichnan–Iroshinikov spectrum of −3/2. Over September 9–10 (panel (d)), two days with less activity, the index in the inertial range was mixed for both $b_\perp$ and $b_{||}$. They both start with index around −1, followed by steepening

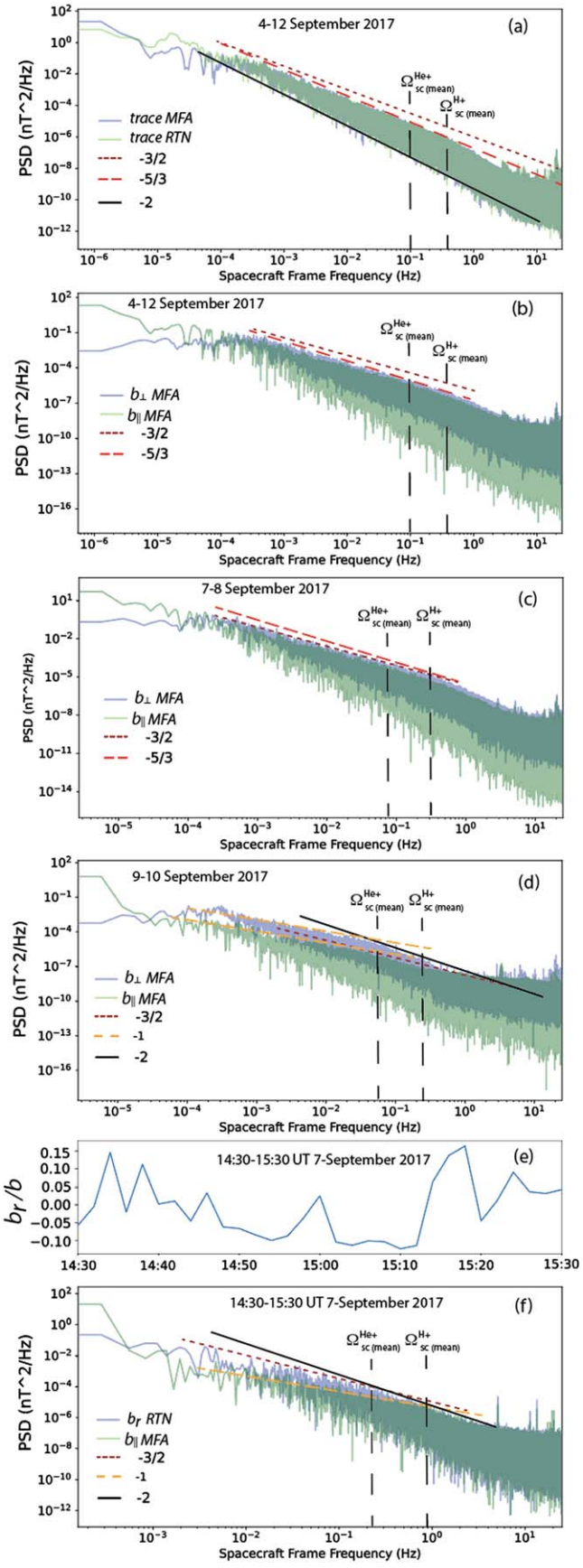


**Figure 3.** The DSCOVR magnetic field PSDs. See the text for explanation.

to $-3/2$ for $b_{||}$, while $b_{\perp}$ was closer to $-2$, then steepened further around $\Omega^{H+}_{sc(mean)}$.

Panel (e) indicates that on September 7, between 14:30–15:30 UT, the IMF was approximately perpendicular $b/b_0 \sim 0$ to the solar wind flow direction. For parallel-propagating waves during this time interval, the wave $k$-vector was also at right angles to the solar wind flow. As a result, the $b_r$ (in RTN) and $b_{||}$ (in MFA) PSDs do not match, as shown in panel (f). Effectively, the IMF rotated about the $T$-axis of RTN, projecting $N$ into the $R$-direction. Hence, the power is higher in $b_r$ compared to $b_{||}$ because the R-component now represents the transverse power. However, the inertial range spectral index for $b_{\perp}$ in both RTN and MFA coordinates for this 1 hr time interval showed no significant differences (results not displayed).

## 6. DSCOVR EMIC Wave Observations

### 6.1. Wave Events

We surveyed the time period September 4–12 for narrow-band EMIC wave intervals by visually inspecting the daily dynamic PSDs and found September 9 and 10 to contain the best waves. Figure 4 shows an example wave event from each day in MFA coordinates. For both events, from the top panel down, we show the $b_{\perp}$ dynamic PSD, the wave ellipticity, the wave normal angle, and the IMF magnitude $b$. The horizontal curves across the spectra represent $\Omega^{H+}_{sc}$ and $\Omega^{He+}_{sc}$.

The wave ellipticity is defined as the ratio of the minor to the major axis of the wave polarization perpendicular to the background magnetic field (Walker 1993). In its simplest form, it can be calculated in Fourier space by taking the real part of the wave $b_y/b_x$ in MFA coordinates, where a value of $-1$ is circular LH polarization, 0 is linear, and $+1$ is RH circular polarization. The wave normal angle defines the angle between the wave k-vector and the background magnetic field (Stix 1992), with 0° and 90° representing parallel and perpendicular propagation, respectively. In practice, the wave normal angle was calculated as the angle between the direction of minimum variance from the complex off-diagonal elements of the spectral matrix and the direction of the background field in the MFA frame (Means 1972).

Transverse wave power dominated on both days. On September 9, almost all the wave power was located below $\Omega^{H+}_{sc}$, indicating LH-polarized EMIC waves. RH-polarized waves were mostly observed above $\Omega^{H+}_{sc}$ at a lower power level. The wave bursts on September 9 generally had low wave normal angles, indicating parallel propagation.

Wave packets were also observed on September 10, again with most of the wave power below $\Omega^{H+}_{sc}$. The wave ellipticity was more mixed for the event on September 10. The strongest wave bursts in the H+ wave band between 09:00–11:00 UT were LH-polarized, but after about 10:10 UT, the polarization switched to RH, albeit at lower power levels.

#### 6.1.1. Wave Modulation

Figure 5 shows the transverse PSD and IMF $b$ time series for a shorter time interval for both the September 9 and 10 EMIC wave events. The vertical dashed lines indicate the alignment of increased wave power with decreases in the background magnetic field. This suggests modulation of the EMIC wave-

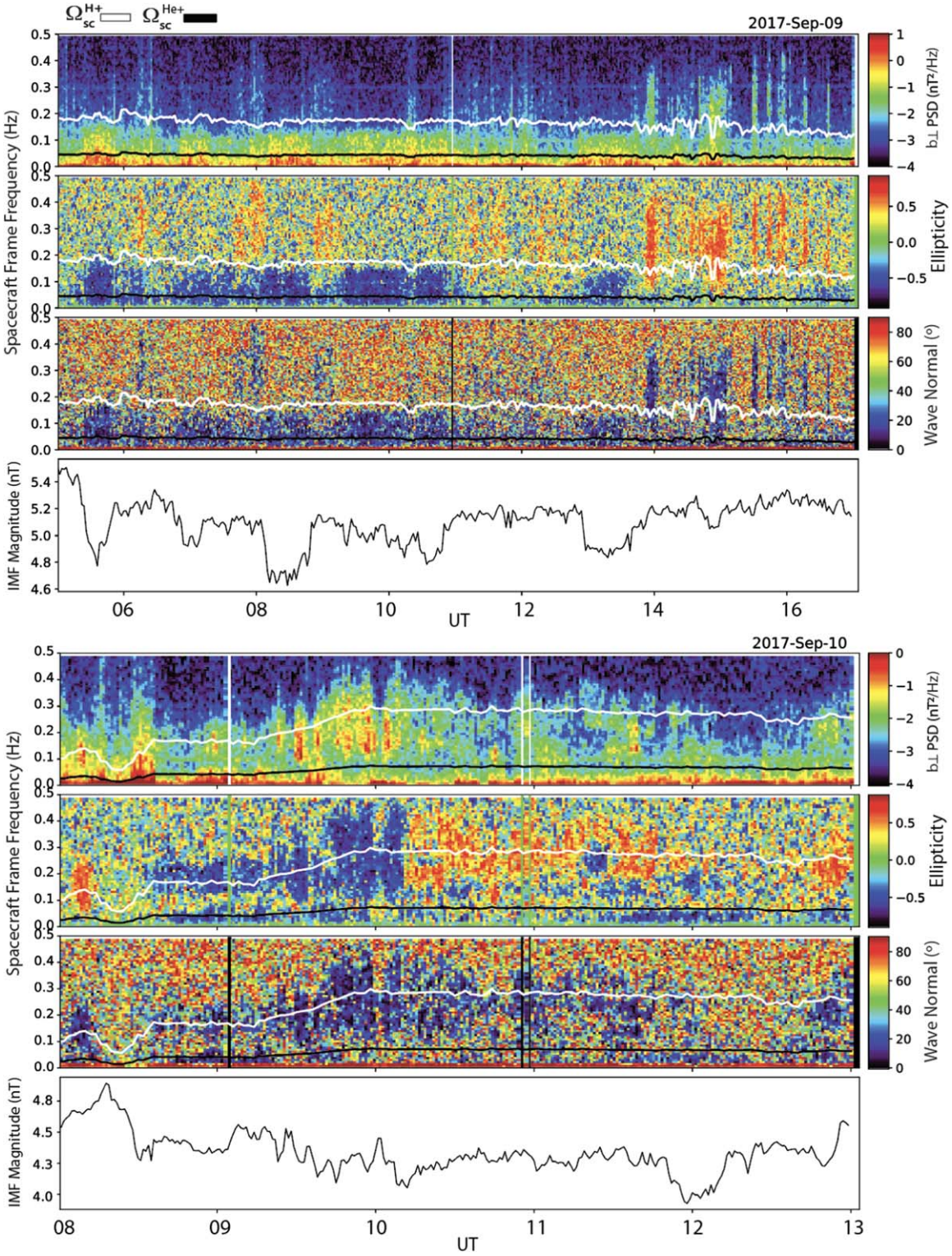


**Figure 4.** Example wave events in MFA coordinates observed on 2017 September 9 and 10. See the text for explanation.

packet generation and/or propagation by longer-period variations in the IMF. Such modulation of the EMIC wave power has been observed in Earth's magnetosphere (Mursula et al. 1997; Loto'aniu et al. 2009; Kakad et al. 2019). In both examples, the modulation would be out of phase, where the higher-frequency wave power increases when there is a decrease in the amplitude of the longer-period wave.

Assuming an H+ ion plasma, for simplicity, the resonant kinetic energy of the interacting protons (Kennel & Petschek 1966) can be written as

$$E_R = \frac{b^2}{2\rho}\frac{1}{X^2}(1 - X)^3, \quad (6)$$

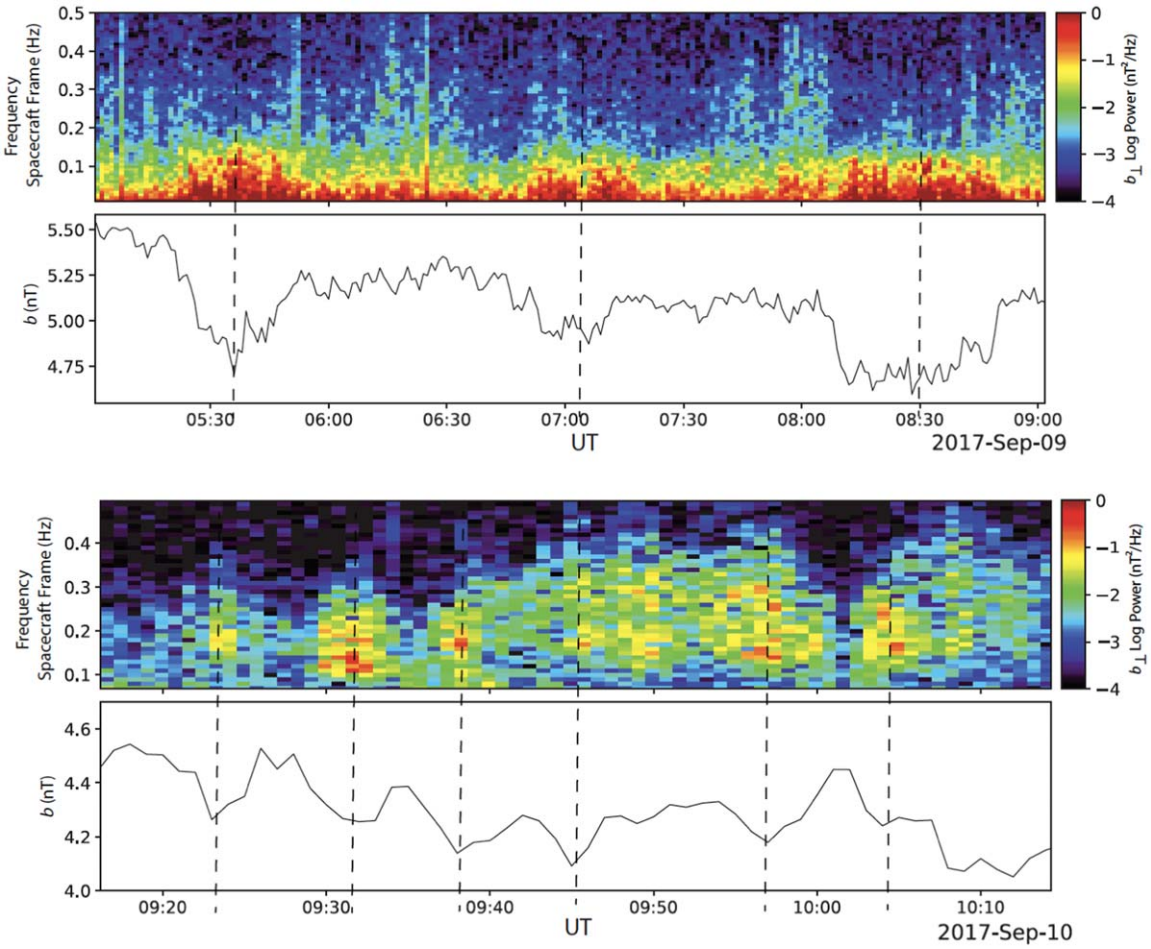


**Figure 5.** Transverse power and background magnetic field for an interval from the September 9 and 10 events. The vertical dashed lines indicate the alignment of increased wave power with decreases in the background magnetic field.

where $X$ is the wave frequency normalized to local H+ cyclotron frequency. In both the Alfvén speed, Equation (3), and resonant energy, Equation (6), we can replace the IMF magnitude $b$ with

$$b = b_0(1 + \delta b), \tag{7}$$

where we define $\delta b$ as a dimensionless parameter within [0, 1], representing the variation in the IMF. A decrease in $b$ results in a decrease in the Alfvén speed, $V_A$, and the resonant energy, $E_R$. A decrease in $E_R$ provides more free energy from energetic ions for cyclotron instability, while the slower wave speed means the wave spends more time in the generation or growth region interacting with this free energy. This is consistent with the antiphase correlation observed in Figure 5 between the longer-period variations in the IMF and bursts in EMIC waves.

In a multi-ion plasma with species $s$, we can follow the derivation by Gail (1990) for parallel-propagating EMIC waves. Since the cyclotron frequency is linear in $b$, we write

$$\Omega_s = \Omega_{s0}(1 + \delta b), \tag{8}$$

with the plasma refractive index as

$$n^2 = n_0^2(1 + N(\delta b)), \tag{9}$$

where $n_0$ is the usual refractive index and

$$N(\delta b) = \left(\sum_{\text{alls}} \Lambda_s \lambda_s \frac{(\pm\lambda_s \delta b - 1)\delta b}{1 \pm \lambda_s \delta b}\right)\left(1 - \sum_{\text{alls}} \Lambda_s \lambda_s\right)^{-1} \tag{10}$$

defines the part of the refractive index due to $\delta b$ variations and

$$\Lambda_s = \frac{\omega_{ps0}^2}{\omega \Omega_{s0}} \tag{11}$$

and

$$\lambda_s = \frac{\Omega_{s0}}{\omega \pm \Omega_{s0}}. \tag{12}$$

Here, $\omega_{ps0}$ and $\Omega_{s0}$ are the unperturbed plasma and ion cyclotron frequency of species $s$, and $\omega$ is the wave frequency. The wavenumber, $k$, can be written as

$$k = \frac{\omega n}{c} = k_0(1 + N(\delta b))^{\frac{1}{2}} \sim k_0\left(1 + \frac{N(\delta b)}{2}\right), \tag{13}$$

where $c$ is the speed of light and $k_0$ is the unperturbed wavenumber. Hence, the wavenumber $k$ is affected by the longer-period $\delta b$ variations. Other plasma parameters, such as the temperature anisotropy and cold plasma density, may be modulated by longer-period waves (Rasinkangas et al. 1994). However, adiabatic interaction between energetic ions and the

longer-period waves would support thermal anisotropy, A, variations that were in phase with long-period oscillations (Gokhberg et al. 1981). The early theoretical study by Coroniti & Kennel (1970), assuming an adiabatic process, considered the modulation of generation parameters of electron whistler waves in the magnetosphere by longer-period waves using the relationship

$$\left(\frac{\partial A}{\partial t}\right)_{\text{adiabatic}} = \frac{1+A}{b_o} \cdot \delta b(t). \quad (14)$$

Kivelson & Southwood (1985) conducted a theoretical study of the relationship between energetic ions and longer-period compressional ultra-low-frequency waves in the magnetosphere, finding that although betatron heating provides ion flux oscillations in phase with variations in the magnetic field, some phase difference does occur between the ion flux oscillations and the magnetic field in the resonant response. Hence, if one considers nonadiabatic processes, EMIC waves may be modulated at varying phase differences with respect to the longer-period waves.

Nonlinear interactions may also be significant. The refractive index in Equation (10) assumes ideal MHD for the long-period waves and quasi-linear theory for the EMIC wave–particle interactions. Gail (1990) also derives the wave temporal growth rate as

$$\gamma \simeq \gamma_0(1 + \Gamma(\delta b)), \quad (15)$$

where $\Gamma(\delta b)$ is the growth rate due to $\delta b$. Gail found that positive growth rates could occur for equilibrium anisotropy that is less than critical anisotropy. Further, Gail suggested that for fixed-equilibrium growth rates, much larger fluctuations in growth rate occur for marginally stable distributions than for unstable distributions. Given a marginally stable region, spectral power overlapping regions may be sufficient to provide EMIC wave growth. In other words, the periodicity of the longer-period modulating wave does not have to match the EMIC wave-packet repetition period.

## 7. Cross-satellite Comparisons

The colocation of Wind, ACE, and DSCOVR at L1 provides opportunities for cross-satellite studies. Unfortunately, Wind is missing data from 2017 September 10. Hence, we only use Wind data for the September 9 event cross-satellite comparisons.

The top two panels in Figure 6 show the spacecraft locations for Wind, ACE, and DSCOVR in GSE ($Re$ = Earth radii units) over the period 2017 September 4–12. Wind is closest to the Sun at Xgse∼262 $Re$, followed by DSCOVR at ∼237 $Re$ and ACE at ∼225 $Re$. The bottom panel of Figure 6 shows the $b_\perp$ trace for ACE (1 Hz data) and DSCOVR (50 Hz data) over 2017 September 4–12 in MFA coordinates. The results for ACE are very similar to those for DSCOVR.

Figures 7(a)–(c) show the $b_\perp$ dynamic PSD in the MFA frame, wave normal angle, and ellipticity for the September 9 events from Wind, DSCOVR, and ACE, respectively. Figures 7(d) and e show the equivalent for the September 10 event, but only for DSCOVR and ACE. The horizontal white lines correspond to the $\Omega_{sc}^{H+}$ locations, with some gaps in the ACE panel due to the low-quality ACE plasma data.

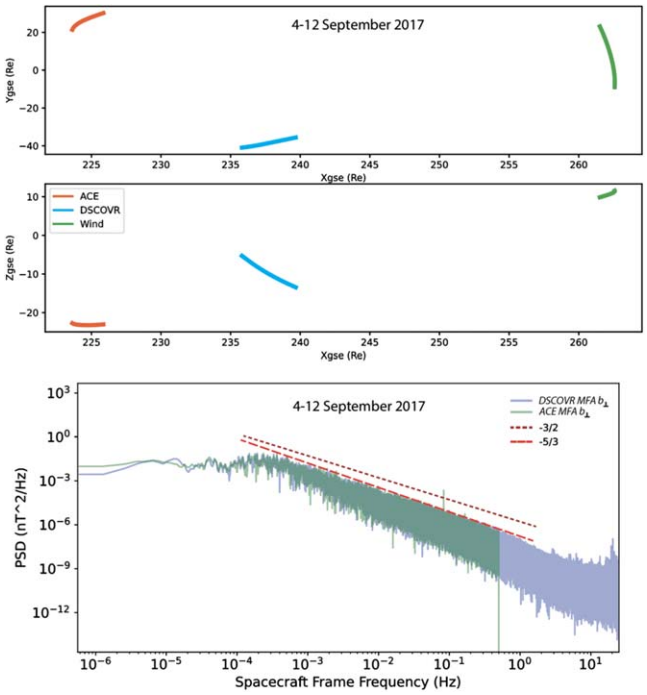


**Figure 6.** The top two panels show the spacecraft locations for Wind, ACE, and DSCOVR in GSE (Earth radii units) over 2017 September 4–12. The bottom panels show a comparison between the ACE and DSCOVR $b_\perp$ trace taken over the same date range as the top panel in MFA coordinates.

On September 9, the dominant wave power was confined below $\Omega_{sc}^{H+}$ for all three satellite observations, particularly for LH-polarized wave bursts, while RH-polarized waves were mostly above $\Omega_{sc}^{H+}$. Like DSCOVR, the LH wave power observed by ACE and Wind tends to occur during decreases in the IMF. For example, for ACE on September 9, there are two bursts of waves centered at 06:00 UT and 12:00 UT, which correlate well with decreases in $b$. However, this was not always the case, as shown by the wave power around 09:00–10:00 UT observed by Wind, with no corresponding $b$ decreases. It should be noted that there is a contamination line around 0.08 Hz in the ACE data and also around 0.3 Hz (shown in red) in the Wind wave normal angle plot. RH-polarized wave power at frequencies $>\Omega_{sc}^{H+}$ are observed by all three satellites in the afternoon UT.

On September 10, both ACE and DSCOVR observed EMIC waves, with the power generally higher at ACE compared to DSCOVR, especially for the H+ band waves between 09:00 and 11:00 UT. The fluctuations in the IMF between about 09:00 and 10:00 UT observed by DSCOVR look different in the ACE data. The edge of the transition from LH to RH mode around 10:09 UT in the DSCOVR data was observed at ACE about 24 minutes later. However, the wave travel time between the satellites would be no more than a few minutes. Hence, the over an order of magnitude increase in wave power from DSCOVR to ACE in the H+ band at about 10:30 UT is a local effect, which corresponds to a dip in $b$ at the ACE location. There is also a decrease in $b$ around 09:37 UT observed by ACE, which is accompanied by a broadening of the wave burst in the dynamic PSD panel. There are other short wave bursts in the ACE PSD data between about 08:50 and 09:23 UT, which do not appear to be associated with $b$.

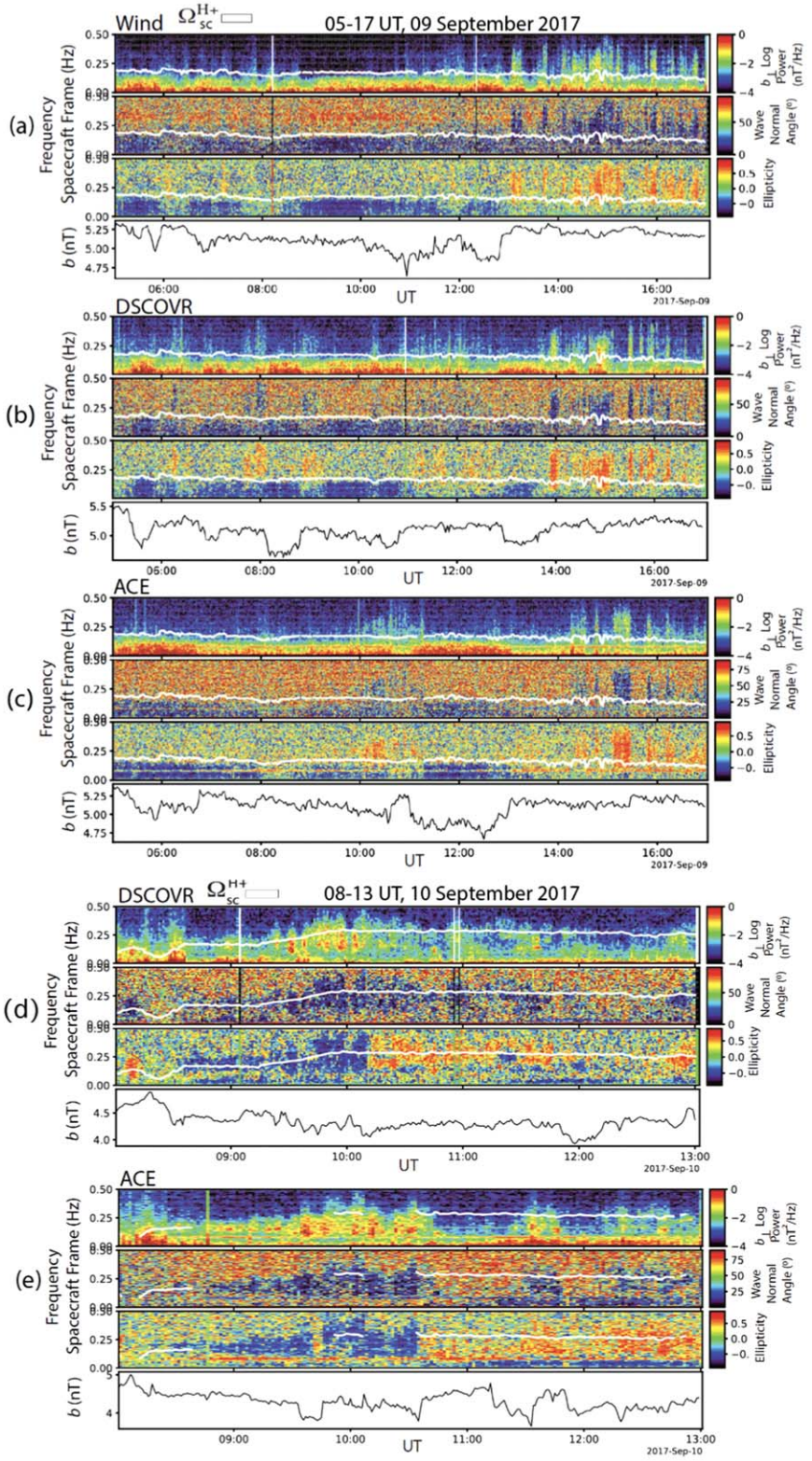


**Figure 7.** Transverse dynamic PSD, wave normal angle, and ellipticity for the September 9 and 10 events. See the text for explanation.

## 8. Stochastic Approach

The observational evidence for turbulent energy cascade in the solar wind mainly comes from determining the spectral index of the solar wind fluctuations. Here we provide an alternative explanation for the observed spectral indices in the inertial range. In the inertial range, we assume that there always exists some containment power that is the result of wave growth and/or propagation. This $1/f$ spectrum is commonly referred to as pink noise or noise that flickers (Barnes & Allan 1966). Furthermore, we assume that the

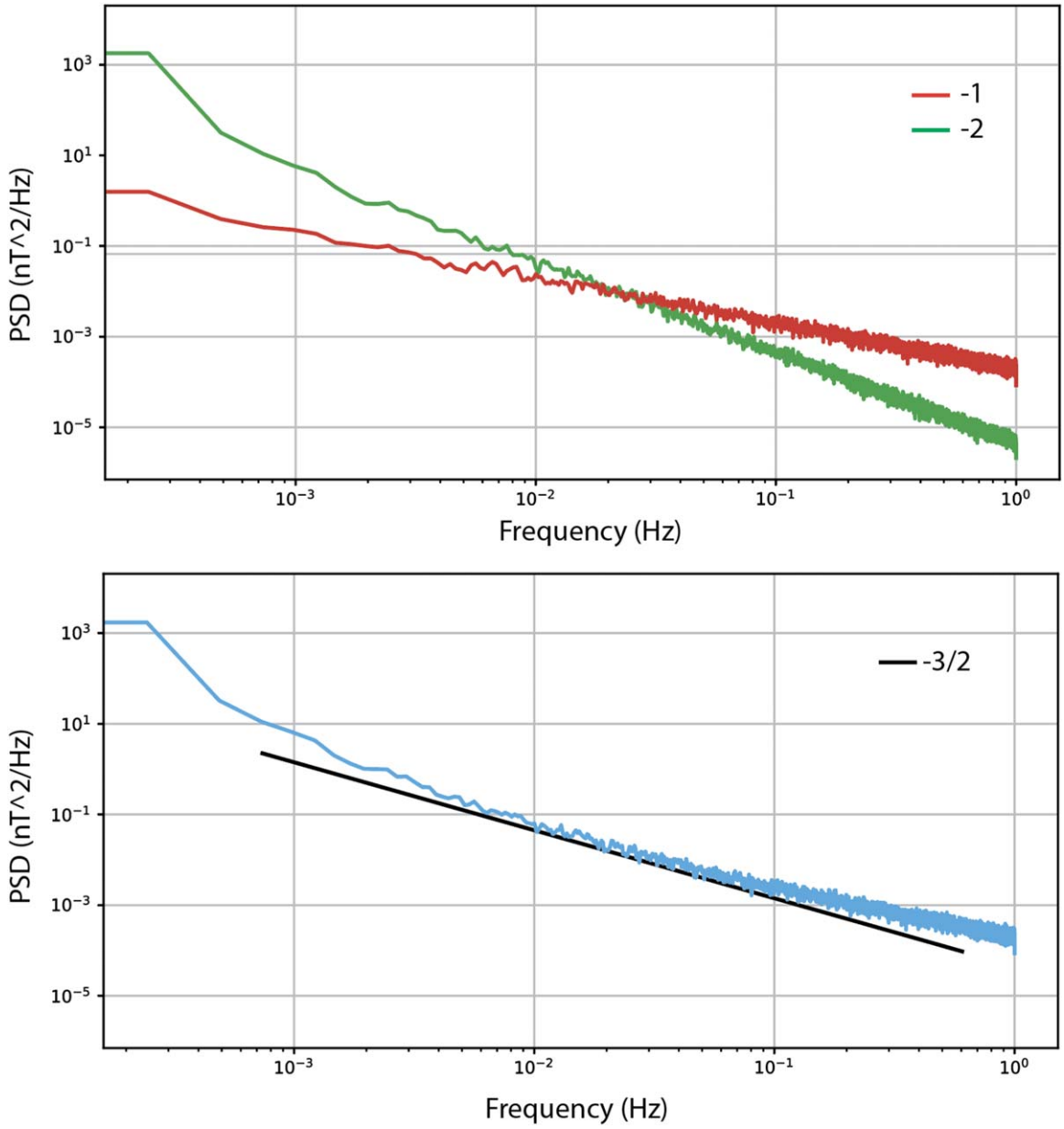


**Figure 8.** The top panel shows the PSD of random signals that have a spectral index of −1 and −2, corresponding to pink noise and stochastic Brownian noise, respectively. The bottom panel shows the PSD of the addition of the two signals in the top panel (in the time domain) and the PSD for a curve with a spectral index of $-3/2$.

remaining signals in the IMF can be considered, over the FFT length, stochastic. This stochastic signal can be written in the form

$$X_t = b_0 \delta b(t), \tag{16}$$

where again $\delta b(t)$ is a time-dependent value in the range [0, 1], but this time representing Brownian motion variations on top of a constant background magnetic field, $b_0$. This makes $X_t$ a random or stochastic signal with a PSD given by

$$PSD_b(f) = \lim_{T\to\infty} \frac{1}{T} E\left\{ \left| \int_0^T e^{\text{ift}} X_t dt \right|^2 \right\}. \tag{17}$$

The value in the curly brackets is the expectation of the Fourier transform of $X_t$. For Brownian motion, the solution (Norton & Karczub 2003) is well known and given by

$$\text{PSD}_b(f) = \frac{4D}{f^2}, \tag{18}$$

where $D$ is the usual diffusion coefficient. Hence, the spectral index for Brownian motion is −2.

In the top panel of Figure 8, we show a simulation of pink-noise and Brownian motion PSDs using the power-law noise algorithm of Timmer & Koenig (1995). The bottom panel shows the resultant PSD when these two signals are added in the time domain. In the region where the power in the two signals is about equal, it is observed that the addition results in a $-3/2$ spectral index. When the containment signal has more power, the index shallows toward −1, while when the Brownian motion PSD is higher, the addition causes a steepening of the index beyond $-3/2$.

In the region where the power from the contaminant and the Brownian motion are equal, the combined PSD can be written as

$$\mathrm{PSD}(f) \propto f^{-\alpha}, \tag{19}$$

where $\alpha$ is given by

$$\alpha = \frac{(\alpha_c + \alpha_b)}{2}, \tag{20}$$

with $\alpha_c$ being the containment index and $\alpha_b$ the index due to Brownian motion. Therefore, we have

$$\alpha = \frac{(\alpha_c + \alpha_b)}{2} = \frac{1+2}{2} = 3/2. \tag{21}$$

A $-3/2$ index is possible simply by assuming the solar wind is composed of equal amounts of power from wave generation and/or containment and stochastic Brownian motion in the inertial range.

## 9. Discussion

It is remarkable that both the spectral trace and the transverse PSD, taken over 9 days, in the inertial range follows **−5/3** (see Figures 3(a)–(b)). This is despite the mixing in the PSD of multiple CMEs and therefore different solar wind features, such as multiple shocks and magnetic clouds. Viall & Borovsky (2020) cautioned against interpreting the spectra without consideration of what specific types of structures are embedded in the solar wind time series.

This caution is warranted, as shown Figure 3(c), with the spectral index during the days that CME1 and CME2 occurred following a Kraichnan–Iroshinikov spectrum, which is inconsistent with the index over the entire 9 days. Studying the spectral indices of different parts of the CMEs is beyond the scope of this study. Previous studies show varying results, with spectral indices near $-1$ in the inertial range having been reported close to the CME bow shock and **−5/3** or steeper inside the CME sheath region (e.g., Hadid et al. 2015). However, Kilpua et al. (2021) did not find evidence of a $-1$ index in the inertial range and instead found the spectral indices in the sheaths to be mostly steeper than **−5/3** and steeper than in the solar wind ahead. Ruzmaikin et al. (1997) found that the CME spectra appeared to be similar to the spectra of the slow wind, i.e., Kolmogorov-like, and that this may be related to both the slow wind and the CME emerging from formerly closed magnetic structures lower in the corona.

Solar wind discontinuities, such as shock fronts from CMEs, can have a significant impact on the energy spectra of the solar wind, complicating interpretation of spectral power and spectral indices (Siscoe et al. 1968; Sari & Ness 1969; Borovsky 2010). The Fourier transform of a discontinuity should produce a $-2$ index, but Borovsky (2010) found that discontinuities in the solar wind could produce spectral indices shallower than $-2$ over a wide frequency range in the inertial range and could even be similar to Kolmogorov and Iroshnikov–Kraichnan indices. They noted that turbulence interpretations of the dynamics and the evolution of the solar wind plasma do not account for the large contribution of strong discontinuities to the power spectra.

The spectral index in the inertial range over September 9–10 (see Figure 3(d)) also does not agree with the 9 days index. September 9–10 was rich in EMIC waves, but with no CMEs, the overall power level on these two days within the inertial range was 1–2 orders of magnitude lower than on September 7–8. EMIC wave activity is the likely cause of the $-1$ containment index observed in $b_\perp$, where evidence of wave cutoff due to the presence of He+ and H+ ions can be seen by the sudden steepening of the index at these ion cyclotron frequencies. The wave cutoff is also observed in the EMIC wave events shown in Figure 4, with the wave power drop-off mostly tracking the location of $\Omega_{\mathrm{sc}}^{\mathrm{H}+}$.

In fact, looking at the dynamic PSD over the entire 9 days shown in Figure 2(e), the $\Omega_{\mathrm{sc}}^{\mathrm{H}+}$ location tracks where the power drops (i.e., the dissipation transition region) closely on most days. For the static PSDs (trace and transverse trace, shown in Figures 3(a)–(b)) over the 9 days, the location of $\Omega_{\mathrm{sc(mean)}}^{\mathrm{H}+}$ also aligns with the transition into the dissipation range. When studying the dissipation range, it is important to use more realistic Doppler shifting, such as Equation (5), that takes into account both density and the $b_r/b$ ratio. Furthermore, when studying active or long time periods, the dynamic PSD shown in Figure 2(e) is a better indicator of the break frequency location, because you can observe how the location varies with time. The days where $\Omega_{\mathrm{sc}}^{\mathrm{H}+}$ is not located at the break frequency location in Figure 2(e) are the highly active CME days. This is likely due to the assumptions used in deriving Equation (5), such as parallel-propagating waves, being overly simplistic for CME periods.

We compared the RTN and MFA coordinates spectral indices in the inertial range and found no significant differences for the trace or transverse trace, which could be interpreted as an indication of isotropic turbulence. However, this was not the case for individual components, as shown in Figure 3(f). When the IMF is perpendicular ($b_r/b \sim 0$), the $b_r$-component (in RTN) is no longer parallel to the IMF, but instead represents one of the transverse components. In interpreting MHD turbulence, it is important to define components relative to the local magnetic field direction (Cho & Vishniac 2000; Milano et al. 2001; Oughton & Matthaeus 2020). The value of $b_r/b$ did not make any difference to the trace indices, which again points to isotropic turbulence.

However, anisotropy was observed on September 9–10 when EMIC waves were observed. Since the power levels in the inertial range were lower on these two days compared to the CME days, it may be that anisotropy is more prominent when overall power levels are lower. Alternately, another way to state this is that when a time series contains both broadband high levels of noise (e.g., due to CMEs) and waves, the containment due to the presence of waves can be hidden or overwhelmed in the resultant PSD by the higher-powered noise. Ion cyclotron waves are commonly observed within the solar wind, while they have also been observed within CMEs (e.g., Ala-Lahti et al. 2019; Dhamane et al. 2023). Since EMIC waves can occur at fractions of the ion cyclotron frequency (e.g., Jian et al. 2009; Wei et al. 2016), it is plausible that the shallow $-1$ index in the $b_\perp$ spectra on September 9–10 extending well below the $\Omega_{\mathrm{sc}}^{\mathrm{He}+}$ location is due to EMIC wave generation within the solar wind through Doppler-shifted ion cyclotron instability.

The observed PSD indices do not agree with the critical balance (CB) argument (Goldreich & Sridhar 1994, 1997). Over the 9 days, the indices for both $b_\perp$ and $b_{||}$ were $-5/3$, while on September 7–8, both were $-3/2$. In the wave–wave modulation mechanism described in Section 6.1.1, CB is not required and instead parameters important for wave–particle

interactions within quasi-linear theory are modulated by lower-frequency variations. There is significant debate within the turbulence community about the observed spectral index for the CB conjecture and even if the CB conjecture holds (Schekochihin 2022). For our mechanism, rather than eddies or nonlinear interactions between counterstreaming Alfvén waves of similar wavelengths resulting in turbulent cascade, the wave–wave interaction affecting the growth rates and propagation characteristics of ion cyclotron waves drains energy from the longer-period fluctuations.

Even if the wave–wave modulation suppresses the EMIC wave growth, energy is still removed from the lower-frequency component, because the modulation itself takes work. In this case, energy goes toward ion heating. The longer-period waves are readily available in the solar wind originating closer to the Sun, including from the CMEs, while over the event time period, the presence of multi-ion species provides plentiful free energy that can be modulated. The **−5/3** and **−3/2** indices are explained by combining containment (−1 index) and Brownian motion (−2 index), with the index being equal to $-3/2$ when there are equal parts of both. At the $\Omega_{sc}^{H+}$ location, kinetic effects dominate, steepening the index below −2. The advantage of our method is that both the inertial and dissipation transition regions are due to the same physical mechanism, i.e., wave–particle interactions.

In hydrodynamic turbulence theory (Kolmogorov 1941), the rate of energy dissipation is equal to the rate of energy cascade across the inertial range. Our mechanism does not require the levels of containment and Brownian motion to be equal. When containment dominates, EMIC waves are likely to be observed, whereas for indices $<-3/2$ (but $\geqslant -2$), stochastic Brownian motion dominates. A stochastic model of IMF fluctuations was presented by Barnes (1981), assuming random changes in the IMF direction. The resultant −2 spectral index from the stochastic model was suggested by Barnes as indicating that observed IMF power-law spectra are consistent with the concept of local random walks. As in our results, Barnes obtained the −2 index by assuming Brownian motion, but Barnes did not include containment in the inertial range.

Not all the ion cyclotron wave packets we observed were associated with longer-period oscillations in the IMF. This may indicate that these wave packets were generated or modulated somewhere else or that their generation and/or propagation characteristics were not related to wave–wave modulation. The wave–wave method of energy transfer only needs to occur regularly enough to account for the rate at which the solar wind energy transfers to smaller scales. How often this wave–wave modulation needs to occur is uncertain, but the rate should be consistent with the PSD index in the inertial range. The stochastic Brownian background can also be viewed as a result of wave–wave modulation, with the parameters important for wave generation/propagation being modulated stochastically.

However, the propagation of energy to a smaller scale through this quasi-linear wave–wave modulation is not a continuous energy cascade, like in turbulence. There can be significant jumps in frequency or k-number. For the September 9 example, the separations between the vertical dashed lines in Figure 5 are about 90 minutes or of the order of $10^{-4}$ Hz, while the EMIC bursts occur with periods of about 10 s or 0.1 Hz. This represents energy transfer across a spectral range of 3 orders of magnitude in one modulation period. For the stochastic background, the occurrence and magnitude of these spectral jumps can be considered random.

In terms of the source of the longer-period variations creating the modulations, for the September 9 example, the approximate $10^{-4}$ Hz modulating wave results in a wavelength of over a million meters, when converting back to the plasma frame and using typical solar wind and Alfvén speeds. Therefore, the wave modulating the higher-frequency EMIC bursts likely originated close to the Sun. In the case of September 10, however, the wave modulation is between 5 and 10 minutes. Taking 7 minutes, we get $2 \times 10^{-3}$ Hz, which in the plasma frame gives about 50,000 m, which more likely originates within the solar wind.

The cross-satellite studies essentially reinforce the findings from DSCOVR. Wave–wave modulation was also suggested from the Wind and ACE observations, while the spectral indices match that observed by DSCOVR. When considering the Alfvén speed, the differences in the wave spectral properties between different spacecraft observations could not in general be explained by wave propagation effects.

It should be noted that we use the words "wave–wave" loosely. This is also true for MHD turbulence, because wave characteristics only last as long as the eddie turnover time (Bruno & Carbone 2013). Plasma instabilities generally emerge from perturbations (Kawata et al. 2019), and therefore low-frequency variability in the solar wind, whether it be waves or magnetic holes or something else, can affect the generation of higher-frequency oscillations and instabilities. Although we focus on EMIC waves, the excitation of any type of shorter-scale instabilities by longer-scale variations may be considered a form of energy transfer to smaller scales.

In the case of quiet solar wind conditions, the observed spectral indices often attributed to turbulence, we argue, are the result of randomly generated higher-frequency variations through wave–wave modulation that have short-lived coherency relative to the FFT length. The stochastic nature of the generation and dissipation of the waves means that the FFT averages out any small or short-lived dumps in the PSD. However, enough containment remains from this wave–wave interaction to flatten the index above the −2 Brownian motion level.

## 10. Conclusions

Using DSCOVR data, we have presented evidence of wave–wave modulation and suggest this as a method of energy cascade in the solar wind. The observed indices between −1 and −2 in the inertial range are not surprising if we assume wave containment combined with stochastic Brownian motion. Previous studies show that fluctuations in the solar wind can be characterized as stochastic, including within CMEs and CIRs (Weygand & Kivelson 2019). In terms of the wave–wave modulation, the length that a wave propagates before encountering the cutoff, crossover, and ion cyclotron frequencies can be thought of as random, due to the variations in plasma parameters that affect critical frequencies. The Doppler-shifted mechanism of the cyclotron instability also means the resonance condition can occur across a range of frequencies below the ion cyclotron frequency. For the often quoted PSD spectral index of $-5/3$, we argue that this occurs because studies tend to concentrate on weak-energy events, where wave generation and containment in the inertial region are weaker, resulting in PSD indices steeper than $-3/2$. Further observational and theoretical studies are required to develop the ideas presented here and determine their full applicability to the evolution of the solar wind.

## Acknowledgments

P.T.M.L. was supported by the NOAA cooperative agreements NA17OAR4320101 and NA22OAR4320151 and by the National Science Foundation grant No. 1931062. L.K. was supported by the National Science Foundation under grant No. 1931062. We wish to thank Brian Kress for the code to plot the GOES-16 SGPS data. The NOAA-NCEI DSCOVR and GOES-R data portals are located at https://ngdc.noaa.gov/dscovr/ and https://www.ngdc.noaa.gov/stp/space-weather/, respectively. The views, opinions, and findings contained in this report are those of the authors and should not be construed as an official National Oceanic and Atmospheric Administration, National Aeronautics and Space Administration, or other U.S. Government position, policy, or decision.

## ORCID iDs

Larisza Krista https://orcid.org/0000-0003-4627-8967

## References

Ala-Lahti, M., Kilpua, E. K. J., Souček, J., Pulkkinen, T. I., & Dimmock, A. P. 2019, JGRA, 124, 3893
Barnes, A. 1981, JGRA, 86, 7498
Barnes, J., & Allan, D. 1966, Proc. Spie, 54, 176
Borovsky, J. E. 2010, PhRvL, 105, 111102
Bowen, T. A., Mallet, A., Huang, J., et al. 2020, ApJS, 66, 246
Bruno, R., & Carbone, V. 2013, LRSP, 10, 2
Chang, T., Crew, G. B., Hershkowitz, N., et al. 1986, GeoRL, 13, 636
Cho, J., & Vishniac, E. T. 2000, ApJ, 539, 273
Cohen, C. M. S., & Mewaldt, R. A. 2018, SpWea, 16, 1616
Coroniti, F. V., & Kennel, C. F. 1970, JGR, 75, 1279
Dhamane, O., Pawaskar, V., Raghav, A., et al. 2023, ApJ, 957, 38
Filwett, R. J., Desai, M. I., Ebert, R. W., & Dayeh, M. A. 2019, ApJ, 876, 88
Gail, W. 1990, JGR, 95, 19089
Gary, S. P. 1993, Theory of Space Plasma Microinstabilities, Cambridge Atmospheric and Space Science Series (Cambridge: Cambridge Univ. Press)
Gokhberg, M. B., Pilipenko, V. A., Pokhotelov, O. A., & Troitskaya, V. A. 1981, JGR, 86, 833
Goldreich, P., & Sridhar, S. 1994, ApJ, 438, 763
Goldreich, P., & Sridhar, S. 1997, ApJ, 485, 680
Gröchenig, K. 2000, Foundations of Time-Frequency Analysis (Applied and Numerical Harmonic Analysis) (Berlin: Springer),
Hadid, L. Z., Sahraoui, F., Kiyani, K. H., et al. 2015, ApJL, 813, L29
He, J., Marsch, E., Tu, C., Yao, S., & Tian, H. 2011, ApJ, 731, 85
Iroshnikov, P. S. 1963, AZh, 40, 742
Jian, L. K., Russell, C. T., Luhmann, J. G., et al. 2009, ApJ, 701, L105
Jian, L. K., Russell, C. T., Luhmann, J. G., et al. 2010, JGRA, 115
Kakad, A., Kakad, B., Omura, Y., et al. 2019, JGRA, 124, 1992
Kawata, S., Karino, T., & Gu, Y. J. 2019, High Power Laser Science and Engineering, Vol. 7 (Cambridge: Cambridge Univ. Press), e3
Kennel, C. F., & Petschek, H. E. 1966, JGR, 71, 1
Kilpua, E. K. J., Good, S. W., Ala-Lahti, M., et al. 2021, FrASS, 7, 109
Kivelson, M. G., & Southwood, D. J. 1985, JGRA, 90, 1486
Kolmogorov, A. N. 1941, DoSSR, 30, 301
Kolmogorov, A. N., Levin, V., Hunt, J. C. R., Phillips, O. M., & Williams, D. 1991, RSPTA, 434, 9
Kraichnan, R. H. 1965, PhFl, 8, 1385
Leamon, R. J., Matthaeus, W. H., Smith, C. W., & Wong, H. K. 1998, ApJ, 507, L181
Loto'aniu, P. T. M., Romich, K., Rowland, W., et al. 2022, SpWea, 20, e2022SW003085
Loto'aniu, T. M., Fraser, B. J., & Waters, C. L. 2009, AnGeo, 27, 121
Mason, G. M., Gold, R. E., Krimigis, S. M., et al. 1998, SSRv, 86, 409
Means, J. D. 1972, JGR, 77, 5551
Milano, L. J., Matthaeus, W. H., Dmitruk, P., & Montgomery, D. C. 2001, PhPl, 8, 2673
Mursula, K., Rasinkangas, R., Bösinger, T., Erlandson, R. E., & Lindqvist, P.-A. 1997, JGRA, 102, 17611
Norton, M. P., & Karczub, D. G. 2003, Fundamentals of Noise and Vibration Analysis for Engineers, 2nd edn. (Cambridge: Cambridge Univ. Press)
Oughton, S., & Matthaeus, W. H. 2020, ApJ, 897, 37
Podesta, J. J., & Gary, S. P. 2011, ApJ, 734, 15
Rasinkangas, R., Mursula, K., Kremser, G., et al. 1994, Solar Wind Sources of Magnetopsheric Ultra-Low-Frequency Waves (Geophysical Monograph Series), Vol. 81 (Washington, DC: AGU), 417
Redmon, R. J., Seaton, D. B., Steenburgh, R., He, J., & Rodriguez, J. V. 2018, SpWea, 16, 1190
Ruzmaikin, A., Feynman, J., & Smith, E. 1997, JGR, 102, 19753
Sari, J. W., & Ness, N. F. 1969, SoPh, 8, 155
Schekochihin, A. A. 2022, JPlPh, 88, 155880501
Siscoe, G. L., Davis Jr., L., Coleman Jr., P. J., Smith, E. J., & Jones, D. E. 1968, JGR, 73, 61
Song, H., Cheng, X., Li, L., Zhang, J., & Chen, Y. 2022, ApJ, 925, 137
Stix, T. H. 1992, Waves in plasmas, https://api.semanticscholar.org/CorpusID:116951042
Szabo, A. 2014, in The 6th NASA Space Weather and Robotic Mission Operations Workshop (Washington, DC: NASA)
Telloni, D., & Bruno, R. 2016, MNRAS, 463, L79
Thorne, R. M., & Horne, R. B. 1994, JGR, 99, 17275
Timmer, J., & Koenig, M. 1995, A&A, 300, 707
Viall, N. M., & Borovsky, J. E. 2020, JGRA, 125, e2018JA026005
Walker, A. D. M. 1993, Plasma Waves in the Magnetosphere (Heidelberg: Springer)
Wei, H. Y., Jian, L. K., Russell, C. T., & Omidi, N. 2016, in Low-Frequency Waves in Space Plasmas, ed. Andreas Keiling, Dong-Hu Lee, & Valery Nakariakov (Washington, DC: AGU), 253
Weygand, J. M., & Kivelson, M. G. 2019, ApJ, 872, 59
Woodham, L. D., Wicks, R. T., Verscharen, D., & Owen, C. J. 2018, ApJ, 856, 49
Zhao, L.-L., Zank, G. P., Adhikari, L., et al. 2020, ApJ, 898, 113